Extended imaging volume in cone-beam X-ray tomography using the weighted Simultaneous Iterative Reconstruction Technique

Joaquim G. Sanctorum[1], Sam Van Wassenbergh[2], Van Nguyen[3], Jan De Beenhouwer[3], Jan Sijbers[3], Joris J.J. Dirckx[1]

1. Laboratory of Biophysics and Biomedical Physics (BIMEF), University of Antwerp, Antwerp, Belgium

2. Laboratory of Functional Morphology (FunMorph), University of Antwerp, Antwerp, Belgium

3. Imec – Vision lab, University of Antwerp, Antwerp, Belgium

Key-words: x-ray tomography, detector-offset, field-of-view, image intensifier, cone-beam

Abstract

An issue in computerized X-ray tomography is the limited size of available detectors relative to objects of interest. A solution was provided in the past two decades by positioning the detector in a lateral offset position, increasing the effective field of view (FOV) and thus the diameter of the reconstructed volume. However, this introduced artifacts in the obtained reconstructions, caused by projection truncation and data redundancy. These issues can be addressed by incorporating an additional data weighting step in the reconstruction algorithms, known as redundancy weighting. In this work, we present an implementation of redundancy weighting in the widely-used Simultaneous Iterative Reconstruction Technique (SIRT), yielding the W-SIRT method. The new technique is validated using geometric phantoms and a rabbit specimen, by performing both simulation studies as well as physical experiments. The experiments are carried out in a highly flexible stereoscopic X-ray system equipped with X-ray image intensifiers (XRIIs). The simulations showed that higher values of CNR could be obtained using the W-SIRT approach as compared to a weighted implementation of SART. The convergence rate of the W-SIRT was accelerated by including a relaxation parameter in the W-SIRT algorithm, creating the aW-SIRT algorithm. This allowed to obtain the same results as the W-SIRT algorithm, but at half the number of iterations, yielding a much shorter computation time. The aW-SIRT algorithm has proven to perform well for both large as well as small regions of overlap, outperforming the pre-convolutional Feldkamp-David-Kress (FDK) algorithm for small overlap regions (or large detector offsets). The experiments confirmed the results of the simulations. Using the aW-SIRT algorithm, the effective FOV was increased by >75%, only limited by experimental constraints. Although an XRII is used in this work, the method readily applies to flat-panel detectors as well.

1. Introduction

An issue concerning digital x-ray detectors is their limited size, therefore limiting the size of objects that can be imaged in radiography or for tomographic reconstruction. For radiography purposes, solutions were provided in the form of semi-automatic (Dewaele *et al* 1999) or automatic (Wang *et al* 2018) x-ray image stitching methods, allowing for an enlargement of the field of view (FOV). This solution is generally not applied to tomographic reconstruction as a more adequate solution was found and developed during the past two decades. It was already shown early on that the diameter of the reconstructed volume could be increased by positioning the detector in a laterally shifted, non-centered position relative to the beam axis and tomographic rotation axis (Cho *et al* 1996). In this way, each recorded projection contains data of at least half the width of the object under consideration, and the effective imaging width is enlarged to a maximum of twice the physical width of the detector, depending on the amount of detector offset (Wang 2002). Yet, adjustments to convenient reconstruction algorithms are necessary to remove the artifacts that are inherent to this detector offset method.

Positioning the detector in a laterally shifted position causes truncation of the image data, which leads to high-frequency components in Fourier space and is one of the sources contributing to artifacts in the reconstruction. This issue was identified and a solution was proposed by introducing an overlap region in the scanning geometry (Cho *et al* 1996), as the overlap region allows for the smoothing of the projection data near the truncated edge. This smoothing turns the edge gradient into a non-singular profile, eliminating the corresponding high-frequency components in Fourier space. However, the overlap region also introduces data redundancy, since parts of the object which lie in this region are imaged over the full 360°, whereas the other parts are imaged over only 180°. Parker introduced a redundant data weighting scheme for short-scan fan-beam CT (Parker 1982) and this concept was adopted to detector-offset tomography to simultaneously correct for data redundancy and truncation edge smoothing. In cone-beam CT, with horizontal rotation stages, data redundancy only occurs in the horizontal midplane, and data redundancy in non-midplanes is assumed as an approximation.

Drawing from the results of Parker, redundancy artifacts have been addressed by introducing a weighting function in the reconstruction algorithms. The redundancy weighting function $w(t)$ generally depends on the horizontal detector coordinate t and provides a smooth transition over the redundancy region between the truncated edge and the uniquely imaged data. In general, the functions have a goniometric form and a zero-gradient on the redundancy region boundary.

First, the redundancy weighting scheme was implemented in analytic methods, such as filtered backprojection (FBP) and FDK (Feldkamp *et al* 1984). Cho *et al.* (Cho *et al* 1996) implemented a weighting scheme in the FDK algorithm in two different ways, before or after the convolution step, referred to as pre-convolutional and post-convolutional weighting. It was shown through simulation studies that a larger overlap region is required for pre-convolutional weighting, thus limiting the obtainable diameter of the reconstructed volume. However, the post-convolutional weighting method is more complex as it needs more preprocessing steps and it introduces more severe shading artifacts for small overlap regions. It was therefore advised to use a moderate overlap region and pre-convolutional weighing, which was later also used by Wang in simulation studies in the field of micro CT (Wang 2002). The results were in agreement with those of Cho *et al*, and the method performed well for different overlap sizes, yielding a flexible way of resizing the detector FOV. Using the weighting function proposed by Wang, Yu *et al*. (Yu *et al* 2004)improved the numerical properties of the reconstruction using a large detector offset (and thus a small overlap region) by converting the weighted cone-beam projection data to equispaced parallel beam data (Yu *et al* 2004). Then, FBP was used to obtain the reconstruction, yielding a suppression of the shading artifacts as opposed to the FDK algorithm. Vedantham *et al*. (Vedantham *et al* 2020) examined the quantitative properties of three different weighting functions (Cho *et al* 1996, Wang 2002, Schäfer *et al* 2011) in a pre-convolutional FDK scheme for cone-beam breast CT. It was found that the results obtained using the different weighting functions were equivalent, which was to be expected as the weighing functions, though having a different formulation, were nearly identical. A comparative study between the use of redundancy weighting in FBP-type and backprojection-filtration-(BPF)-type methods was conducted by Schäfer *et al*. (Schäfer *et al* 2011), which showed that BPF-type methods have the potential of providing better image quality for small redundancy regions, while FBP-type methods were superior in the case of larger overlap regions.

Besides analytical reconstruction methods, redundancy weighting schemes have also been implemented in iterative algorithms. Hansis *et al.* reported the use of redundancy weighting in two different iterative reconstruction schemes: Ordered Subset Simultaneous Algebraic Reconstruction Technique (OS-SART) and Maximum Likelihood Ordered Subset Separable Paraboloidal Surrogates (ML OS-SPS) (Hansis *et al* 2010). Instead of applying the sinusoidal weighting directly to the raw projections, it was applied to subsets of opposite correction projection pairs that contribute to the update of the same voxel, where the correction term is normalized on a voxel level. This way, the unit sum criterion of the weights ($w(t) + w(-t) = 1$) as stated by Parker was circumvented, granting more freedom in the choice of $w(t)$. It was shown that, for a small redundancy region, their approach (both SART and ML) yielded better results in terms of image uniformity (less shading artifacts) as compared to FDK. Bian *et al.* implemented the redundancy weighting scheme in two optimization methods (ASD-WPOCS and EM) for sparse data tomography (Bian *et al* 2012). They found that their ASD-WPOCS method produced superior results in terms of streak artifact mitigation and low-contrast details as opposed to EM or FDK, opening up possibilities for dose reduction in detector-offset CBCT. In the field of micro CT, Sharma *et al.* implemented the redundancy weighting in a hybrid reconstruction scheme to merge the benefits of post-convolutional weighted FDK and weighted SART in terms of low- and high-frequency contributions, suppressing shading artifacts in the reconstruction (Sharma *et al* 2014).

The standard reconstruction technique used in medical cone-beam systems is the FDK algorithm, due to its speed and ease of use. However, the FDK algorithm only provides reliable results for perfectly circular projection tracks, and can therefore not be used in highly modular imaging systems (unless a specific modification to the FDK algorithm is implemented for each change of geometry). Therefore, we propose the first implementation of the redundancy weighting scheme in the Simultaneous Iterative Reconstruction Technique (SIRT), as it can handle more complex geometries easily and is thus widely applicable. The performance of the weighted SIRT (W-SIRT) algorithm is compared to the pre-convolutional weighted FDK algorithm and a weighted SART (W-SART) implementation. We will consider the practical implications of using the detector offset method in a highly modular set-up to estimate the maximum gain in effective detector width. The proposed algorithm will be experimentally validated using physical geometric phantoms and a rabbit specimen.

2. Methods

2.1 Redundancy weighting

Positioning the detector in a lateral offset position causes the projections to be width-truncated and to contain redundant data in the vicinity of the projected position of the rotation axis, which is schematically visualized in figure 1. Both of these issues can be solved by introducing a redundancy weighting function $w(t)$ in the reconstruction algorithm. Such a function should assume a value of one within the range of the detector outside of the redundancy region and a value of zero out of the range of the detector. Within the redundancy region, the function should provide a smooth transition from zero to one, where the unit sum of the weights is to be respected ($w(t) + w(-t) = 1$). At the edges of the redundancy region, the

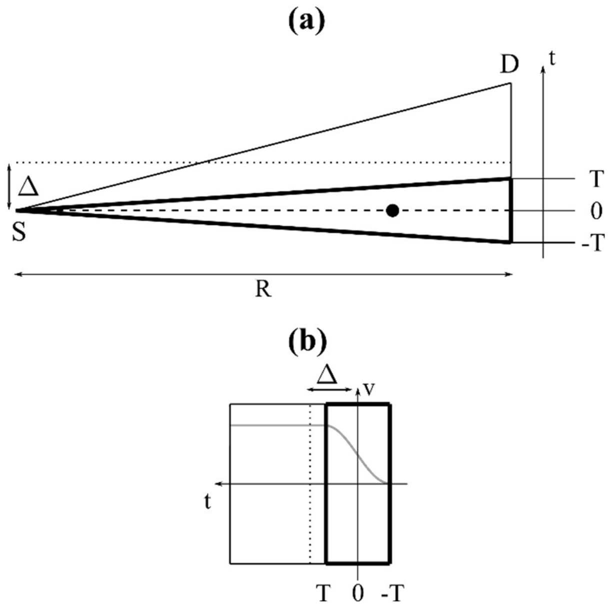

Figure 1: **(a)** Schematic representation (top view) of a detector surface (D) being placed in a lateral offset position with respect to the line connecting the position of the rotation axis (thick black dot) and the source (S), which is represented by a dashed line. The center of the detector is depicted using a dotted line, and the offset value is denoted as Δ. The thick line represents the part of the cone in which redundant data is recorded, corresponding to the horizontal detector coordinate $t \in [-T, T]$. The distance between the source and the detector surface equals R. **(b)** Front view of the detector surface introducing verticle detector coordinate v. The same symbols as in **(a)** apply. The thick gray line shows the typical shape of the redundancy weighting function, varying smoothly from 0 to 1 from $-T$ to T.

derivative should be zero. A function that meets these demands was proposed by Wang *et al.* and will be used further on in this manuscript (Wang 2002):

$$w_{wang}(t) = \begin{cases} 0 & , \quad t < -T \\ \frac{1}{2}\left[sin\left(\frac{\pi\, atan\left(\frac{t}{R}\right)}{2\, atan\left(\frac{T}{R}\right)}\right) + 1\right] & , \quad -T \leq t \leq T. \\ 1 & , \quad t > T \end{cases} \tag{1}$$

In the former expression, t is the horizontal detector coordinate. The value T marks the redundancy region as depicted in figure 1 and R represents the distance between the source and the detector surface. The typical shape of the weighting function is shown in figure 1**(b)**.

2.2 W-SIRT implementation

In general, algebraic reconstruction methods are based on solving the following linear system of equations:

$$\boldsymbol{Ax} = \boldsymbol{p}, \tag{2}$$

where $\boldsymbol{x} \in \mathbb{R}^n$ is a voxelized model of the volume of attenuation coefficients to be reconstructed, which is transformed in a set of log-corrected projections $\boldsymbol{p} \in \mathbb{R}^m$ by the projection matrix $\boldsymbol{A} \in \mathbb{R}^{m \times n}$ that represents the relative contributions of the rays to each pixel of the projections. A trivial way of solving this equation is by inversion of the matrix $\boldsymbol{A}$. However, the matrix $\boldsymbol{A}$ is generally not a square matrix, implying the non-existence of its inverse. Moreover, the huge size and sparsity of the matrix $\boldsymbol{A}$ do not allow for matrix inversion, and therefore, iterative methods are used to estimate the volume $\boldsymbol{x}$ by minimizing the difference between the recorded projections $\boldsymbol{p}$ and the estimated projections $\boldsymbol{Ax}$. One of such iterative methods, which solves a weighted least-squares problem, is the Simultaneous Iterative Reconstruction Technique (SIRT) (Kak and Slaney 1988):

$$\forall j = 1,2, \dots N : x_j^{(k+1)} = x_j^{(k)} + \alpha \frac{\sum_{i=1}^{M} \left[a_{ij} \frac{\left(p_i - \sum_{h=1}^{N} a_{ih} x_h^{(k)}\right)}{\sum_{h=1}^{N} a_{ih}} \right]}{\sum_{i=1}^{M} a_{ij}}. \quad (3)$$

The factor α is a relaxation parameter that equals 1 in the regular SIRT algorithm. This update scheme is often presented in its matrix notation by defining $\boldsymbol{x} = [x_j]$, $\boldsymbol{p} = [p_i]$, $\boldsymbol{A} = [a_{ij}]$, $\boldsymbol{R} = [r_{ij}]$, and $\boldsymbol{C} = [c_{ij}]$:

$$\boldsymbol{x}^{(k+1)} = \boldsymbol{x}^{(k)} + \boldsymbol{C}\boldsymbol{A}^T\boldsymbol{R}\left(\boldsymbol{p} - \boldsymbol{A}\boldsymbol{x}^{(k)}\right), \quad (4)$$

where $\boldsymbol{R}$ and $\boldsymbol{C}$ are diagonal matrices containing the inverted row and column sums, $r_{ii} = 1/\sum_{j=1}^{N} a_{ij}$ and $c_{jj} = 1/\sum_{i=1}^{M} a_{ij}$, respectively. It can be proven that in this form, the convergence of the SIRT algorithm is guaranteed (Gregor and Benson 2008). In this iterative scheme, the redundancy weighting can be implemented prior to the backprojection step (multiplication by $\boldsymbol{A}^T$) by introducing the diagonal weighting matrix $\boldsymbol{W}$, of which the diagonal elements correspond to the correct weighting factors calculated using equation (1).

$$\boldsymbol{x}^{(k+1)} = \boldsymbol{x}^{(k)} + \boldsymbol{C}\boldsymbol{A}^T\boldsymbol{R}\boldsymbol{W}\left(\boldsymbol{p} - \boldsymbol{A}\boldsymbol{x}^{(k)}\right). \quad (5)$$

We thus obtain the weighted SIRT, or W-SIRT, update scheme, which shall be evaluated using different study objects. As the matrix $\boldsymbol{W}$ only contains values from zero to one on its diagonal (which are thus its eigenvalues), convergence is still guaranteed. Reconstructions are carried out using the 1.9.0.dev11 version of the ASTRA toolbox (Aarle *et al* 2016) in a Matlab (Mathworks, Massachusetts, USA) environment (version 2019b). To assess the convergence rate of the proposed method, the weighted residual norm (RN) is calculated after each iteration. The norm is calculated as $\|\boldsymbol{A}\boldsymbol{x} - \boldsymbol{p}\|_R$ with $\|\boldsymbol{A}\boldsymbol{x} - \boldsymbol{p}\|_R^2 = (\boldsymbol{A}\boldsymbol{x} - \boldsymbol{p})^T R\ (\boldsymbol{A}\boldsymbol{x} - \boldsymbol{p})$. The method will be evaluated using some quantitative measures, such as root-mean-square contrast (or RMS contrast, C_{RMS}), contrast-to-noise ratio (CNR), root-mean-squared error (RMSE), and total computation time.

The contrast in the reconstructed volumes will be assessed using the RMS contrast C_{RMS}, calculated as

$$C_{RMS} = \sqrt{\frac{1}{N}\sum_{j=1}^{N}\left(x_j - \overline{\boldsymbol{x}}\right)^2}\,, \tag{6}$$

where N is the number of voxels in the reconstructed volume and $\overline{\boldsymbol{x}}$ is the mean value of the reconstructed volume. The CNR is calculated as the difference between mean gray values in equally-sized, homogeneous regions in the signal and the noise divided by the standard deviation of that noise region:

$$CNR = \frac{\mu_{signal} - \mu_{noise}}{\sigma_{noise}}, \tag{7}$$

wherein μ stands for mean and σ stands for standard deviation. In the simulations, RMSE between the reconstructed volume and the original phantom is calculated as

$$RMSE = \sqrt{\frac{1}{N}\sum_{j=1}^{N}\left(x_j^{rec} - x_j^{pha}\right)^2}, \tag{8}$$

with N the total number of voxels in the reconstructed volume. The superscripts ‘rec’ and ‘pha’ stand for ‘reconstructed volume’ and ‘phantom’, respectively. Reconstruction times are measured by Matlab.

2.3 Simulations

Prior to physical experiments, the W-SIRT algorithm is compared to the pre-convolutional weighted FDK algorithm and the weighted SART-TV (W-SART-TV) method presented earlier by Sharma *et al*., referred to as ‘WIR’ in their work. (Sharma *et al* 2014). Following the work of Sharma *et al*, the TV denoising is performed using gradient descent. The phantom used in the simulations is a slightly elongated version of the 3D Shepp-Logan phantom (Shepp and Logan 1974) of size 1341 voxels × 678 voxels × 283 voxels with a voxel size of ≈ 0.143 mm. The goal of the simulations is to compare the methods in terms of convergence rate, reconstruction time, and the CNR and RMSE of the reconstructed slices for both a large and a small overlap region. Furthermore, we assess the performance of the WIR method without applying TV denoising to the reconstructed volume, referred to as weighted SART or W-SART. Finally, the possibility of speeding up the W-SIRT method is investigated.

Using the ASTRA toolbox, 450 forward projections of the voxel model were obtained over 360° by applying the forward projection operators. In the projection geometry, a conical x-ray beam was used of which the angle is automatically set by ASTRA to cover the full extent of the detector. The detector was chosen to have 2048 pixels in the t-dimension and 700 pixels in the v-dimension. Gaussian noise and blur were added to the projections, as it was shown in our previous work that this is in good agreement with the noise and blur characteristics of our real detectors (Sanctorum *et al* 2020a). The geometry parameters in the simulations, found in table 1, were chosen to correspond to the physical parameters of the set-up. To simulate the detector offset, the projection data was truncated in the t-dimension. First, 800 pixels were truncated to simulate an overlap region of 448 pixels (or 63.9 mm). Then, 1000 pixels were truncated, resulting in an overlap region of 48 pixels (or 6.8 mm). The overlap region is different in size, but the size of the FOV remains the same (292 mm). To examine the difference between the convergence rate using a centered detector and an offset-positioned detector, reconstructions are also made using the full, non-truncated projection data. For the assessment of the methods, only the central slice was reconstructed.

Table 1: Simulation parameters

phantom	SRD (mm)	DRD (mm)	$2T$ (mm)	N_p	N_t	N_v
Shepp-Logan	1770	230	63.9	450	2048	700
Shepp-Logan	1770	230	6.8	450	2048	700

The distances from the source to the rotation axis and from the detector to the rotation axis are denoted as SRD and DRD, respectively. The width of the overlap region is defined as $2T$ (see figure 2). For each set dataset, 450 projections (N_p) were sampled over 360°. The number of detector pixels in both dimensions is given by N_t and N_v, respectively.

2.4 Image acquisition

The radiographs were recorded using the stereoscopic 3D²YMOX (3D DYnamic MOrphology using X-rays) imaging system (Sanctorum *et al* 2019) (figure 2). The recorded images consist of 2048 pixels × 2048 pixels covering a FOV of 292 mm × 292 mm (pixel size ≈ 0.143 mm). To rotate the samples, a custom-made rotation stage was used. A frequency-controlled asynchronous motor, equipped with a factor 40 gearbox, allows the top platform to make a complete revolution in ~2 s, during which the projection data is continuously recorded with a shutter time of 0.5 ms. As the 3D²YMOX system is highly modular (all components can be translated and rotated independently), there is a continuous range of possible detector offset, but every modification of the set-up requires a calibration of the system's geometry, for which a method developed by Nguyen *et al*. was applied (Nguyen *et al* 2021). Since the images are recorded using XRIIs, geometric distortion is present in every frame, deteriorating the accuracy of the geometry calibration and the quality of the tomographic reconstruction. A method developed earlier by Sanctorum *et al*. was used to remove the distortion from the images prior to geometry calibration and subsequent reconstruction (Sanctorum *et al* 2020a, 2020b).

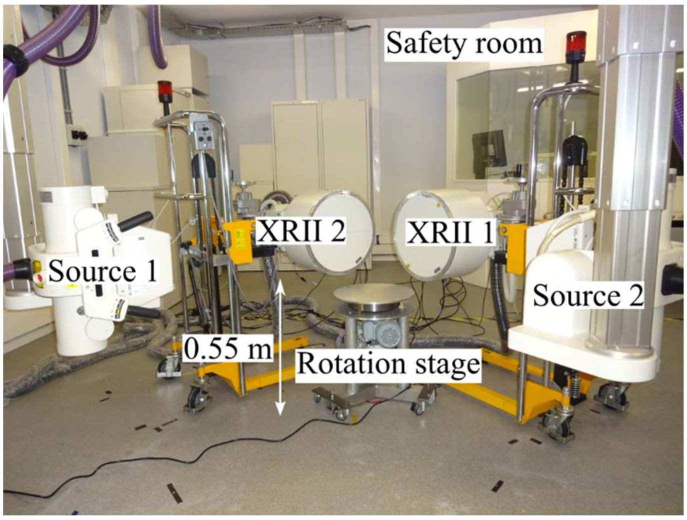

Figure 2: The stereoscopic 3D²YMOX system. The X-ray sources are attached to ceiling gantries, whereas the XRIIs are mounted on hydraulic trolleys. In the middle, the rotation stage is shown. The height of the rotation stage is provided to indicate the dimensions of the set-up.

2.5 Experiments

2.5.1 LEGO phantom

The first experiments were carried out using a test phantom built of LEGO bricks (figure 3(a)), with dimensions of 183 mm × 128 mm × 76 mm. The phantom was built to fit within the FOV of a centered detector. This way, the reconstructions obtained with an offset-detector and the W-SIRT algorithm can be compared to those of a regular SIRT reconstruction (centered detector). To validate our proposed method for different sizes of overlap regions, the detector was manually set in four different offset positions, varying between 0 mm and 100 mm in steps of approximately 25 mm.

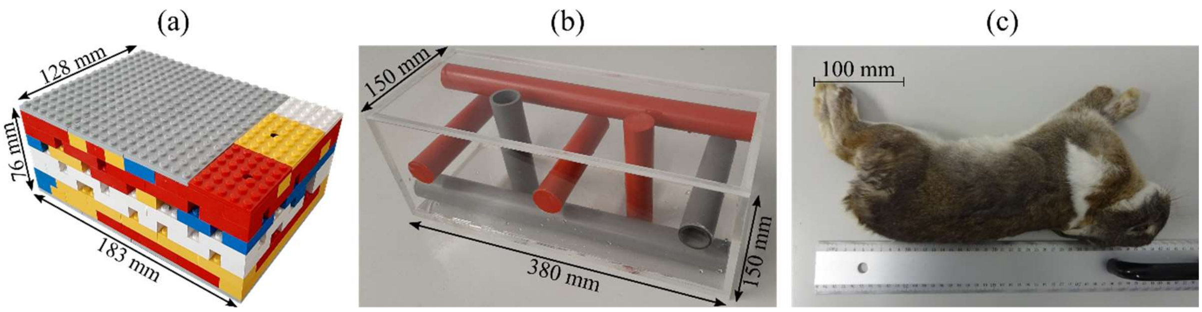

Figure 3: Used study objects. **(a)** LEGO phantom. **(b)** PMMA phantom containing PVC tubes. **(c)** Frozen rabbit specimen.

After each manipulation of the geometry, it is indispensable to record a dataset to calibrate the geometry of the set-up. For geometry calibration, a method developed by Nguyen *et al*. is used (Nguyen *et al* 2020, 2021). The amount of detector shift can be extracted from the calibration results, which will be used to calculate the resulting effective FOV.

The purpose of the LEGO phantom is mainly to examine the difference in convergence rate, reconstruction quality, and computation time for a centered reconstruction and reconstructions obtained with different detector offset values. The phantom contains three gear-shaped objects at different heights and different distances from the center of the phantom that have homogeneous regions suitable for CNR calculations. Besides the quantitative analysis using the CNR and the C_{RMS}, the reconstructed volumes will be compared visually. In these analyses, the W-SIRT algorithm is compared to the W-SART algorithm. Table 2 shows the conditions under which the radiographs of the phantom were recorded. The phantom was positioned on the rotation stage resting on its largest surface with the studs of the LEGO bricks pointing upwards, as in figure 3**(a)**.

2.5.2 PVC tube phantom

To validate the method on a sample of which the size exceeds the width of the detector, a phantom containing PVC tubes was built, which is shown in figure 3**(b)**. The PVC tubes are mounted in a case of PMMA (thickness of 5 mm) of which the outer dimensions are 380 mm × 150 mm × 150 mm. The long PVC tubes have lengths of 370 mm, whereas the short tubes have lengths of 140 mm. All tubes have an outer diameter of 31.7 mm, but the gray tubes are hollow whereas the red tubes are solid. The PMMA case has a removable lid, so the phantom can be filled with, for example, water. To record the projections, the phantom was placed on the rotation stage with the three short horizontal tubes parallel to the floor. First, the phantom was imaged in an empty state (filled with air), then it was imaged again filled with water. The imaging conditions can be found in table 2.

2.5.3 Rabbit

To validate our proposed method on a biological sample of which the dimensions are too large to be imaged with a centered detector, we recorded data of a rabbit specimen. The specimen was borrowed from the veterinary sciences department of the University of Antwerp, where it was sacrificed earlier for other research purposes unrelated to this work and was delivered to us in a frozen state. As shown in figure 3**(c)**, the rabbit had a horizontal span of more than 40 cm. The effective span of the rabbit as projected on the detector was larger than 45 cm due to the magnification factor of 1.13 (see table 2 for scanning information), vastly exceeding the physical size of our detector (292 mm). During the acquisition, the rabbit was positioned on the rotation stage on its side, as viewed from above in figure 3**(c)** (rotation axis through its flanks). The imaging parameters are found in table 2.

Table 2: Experimental scanning information

	LEGO phantom	Tube phantom (air)	Tube phantom (water)	Rabbit
SRD (mm)	1248	1762	1762	1762
DRD (mm)	237	230	230	230
I (mA)	40	40	10	44
V (kV)	60	70	86	70
N_p	450	450	450	450
$\Delta\theta$ (°)	0.4	0.4	0.4	0.4
Δt (ms)	0.5	0.5	0.5	0.5

For each of the conducted experiments, the data acquisition parameters are presented. The distance from the source to the rotation axis (SRD), as well as the distance from the detector to the rotation axis (DRD) are given. The tube current (I) and voltage (V) are also shown. The number of recorded projections, the angular interval between the projections, and the shutter time are denoted as N_p, $\Delta\theta$, and Δt, respectively.

3. Results

Prior to showing the results, it needs to be mentioned that when reconstructed slices or gray value profiles are shown, the gray values originate from the raw reconstructed volume, without any postprocessing. This means that the gray values in the reconstructed volumes are not converted to integers or Hounsfield units. This implies that the gray values of a slice of a line profile windowed between two values do not only assume the integer values in between, but also decimal values.

3.1 Simulation results

In the simulations, the reconstructed slice had a size of 1440 voxels × 780 voxels with a voxel size of 0.143 mm. First, the convergence rate of the proposed W-SIRT method was examined by calculating the residual norm after each iteration. This was also done for the W-SART and W-SART-TV methods. In figure 4, the convergence curves are shown for 350 iterations of each method (panel **(a)**) for a centered detector and for an overlap region of $2T = 63.9$ mm. Panel **(b)** shows the residual norm of the last 150 iterations to increase visibility.

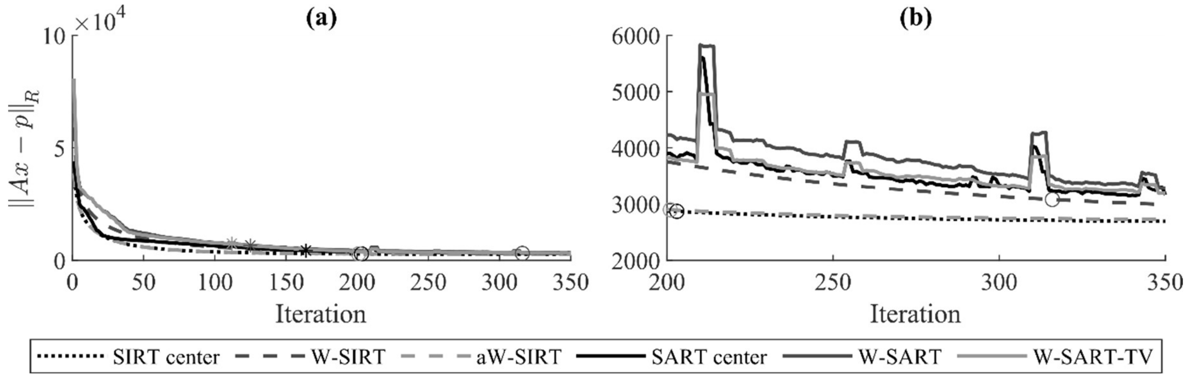

Figure 4: **(a)** Convergence curves for the iterative methods under consideration for a detector overlap of $2T = 63.9$ mm and for a centered detector (indicated by the word 'center' in the legend). On the curves, the number of iterations for which convergence can be claimed are marked a 'o' and a '*' symbols for the SIRT and SART methods, respectively. $(\boldsymbol{b})$ Final 150 iterations of the curves in **(a)** to illustrate the differences invisible in **(a)**.

It is shown in panel **(a)** that for a centered detector, the SIRT and SART algorithms (both not weighted) converge at roughly the same rate during the early iterations. However, during the later iterations, it is seen that the SIRT algorithm converges faster and that the convergence curve is more stable. When a laterally shifted detector is used, it is apparent that the W-SIRT algorithm converges slower than in the case of a centered detector, and the same is true for the W-SART method in comparison to the centered SART method. By including TV denoising in the W-SART method, the convergence curve of centered SART is approximated in the later iterations. The W-SIRT algorithm catches up with the centered SART algorithm after approximately 50 iterations and it is shown in panel **(b)** that the W-SIRT method converges faster than de SART variants.

It is undesirable for the SIRT algorithm to converge slower in case the detector is put in an offset position, as this implies that more iterations are necessary to reach convergence, which is time-consuming. We therefore aim to accelerate the convergence rate of the W-SIRT algorithm by incorporating the relaxation parameter α of equation (3) in equation (5):

$$\boldsymbol{x}^{(k+1)} = \boldsymbol{x}^{(k)} + \alpha \boldsymbol{C}\boldsymbol{A}^T \boldsymbol{R}\boldsymbol{W}\left(\boldsymbol{p} - \boldsymbol{A}\boldsymbol{x}^{(k)}\right). \tag{9}$$

It was previously shown (Gregor and Benson 2008) that the convergence rate of the SIRT algorithm could be increased by choosing the value of α to lie between 1 and 2. In the work of Gregor and Benson it is stated that a value of $\alpha = \frac{2}{1+\epsilon}$ with $\epsilon \leq 0.005$ could double the rate of convergence, given it would lead to a correct bound on the minimum eigenvalue of the matrix $\boldsymbol{C}\boldsymbol{A}^T\boldsymbol{R}\boldsymbol{A}$. Therefore, we have chosen the value of $\epsilon = 0.005$, resulting in $\alpha = 1.99$ in equation (9). The weighted SIRT method corresponding to equation (9) with the given α will be referred to as accelerated W-SIRT, or aW-SIRT, from now on. On both panels of figure 4, it is shown that the aW-SIRT algorithm indeed converges faster than the regular W-SIRT algorithm and that its convergence curve approximates the one of the centered, not-weighted SIRT algorithm.

Based on our data, a suitable criterion to claim convergence would be to state that the RN drops below 10% of its original value while the relative difference between two subsequent RNs, calculated as $\Delta RN_i = \frac{RN_{i-1} - RN_i}{RN_{i-1}}$ with i the iteration number, drops below 0.1%. These convergence points are indicated in figure 4 using 'o' and '*' symbols for the SIRT and SART methods, respectively. In table 3, the exact number of iterations N_{it} for which convergence is reached is shown for each of the methods, along with the average time per iteration Δt_{it}, for the curves in figure 4.

Table 3: Convergence overview

Method	N_{it}	Δt_{it}
Centered SART	164	0.102
W-SART	125	0.102
W-SART-TV	112	0.266
Centered SIRT	203	0.128
W-SIRT	316	0.129
aW-SIRT	201	0.130

Number of iterations N_{it} and average time per iteration Δt_{it} for the curves shown in figure 4.

From table 3, it would seem that the SART methods converge at a faster rate than the SIRT methods. However, figure 4 shows that on the points where convergence could be claimed based on the criterion, the SART methods actually have not converged yet. In the SART methods, it is possible that a single iteration does not bring much new information, and therefore the RN barely alters, resulting in a small ΔRN_i. This does not occur for the SIRT methods, and the convergence claim is more reliable. Therefore, we have chosen to run the same number of iterations in the SART methods as in the W-SIRT method, as these curves are the most alike. Table 3 additionally shows that the time per iteration is generally smaller when using SART or W-SART, but the additional TV denoising tremendously increases the computation time.

In figure 5, central slice reconstructions of the 3D Shepp-Logan phantom are shown for the different reconstruction methods, being pre-convolutional FDK and the SIRT and SART variants described earlier. The number of iterations for each method was chosen based on the convergence criterion (table 3). In the first column, the typical artifacts related to an off-centered detector are shown. These have the form of bright circular artifacts, marking the overlap region. However, as is shown in the ROI images below the full slices, these artifacts

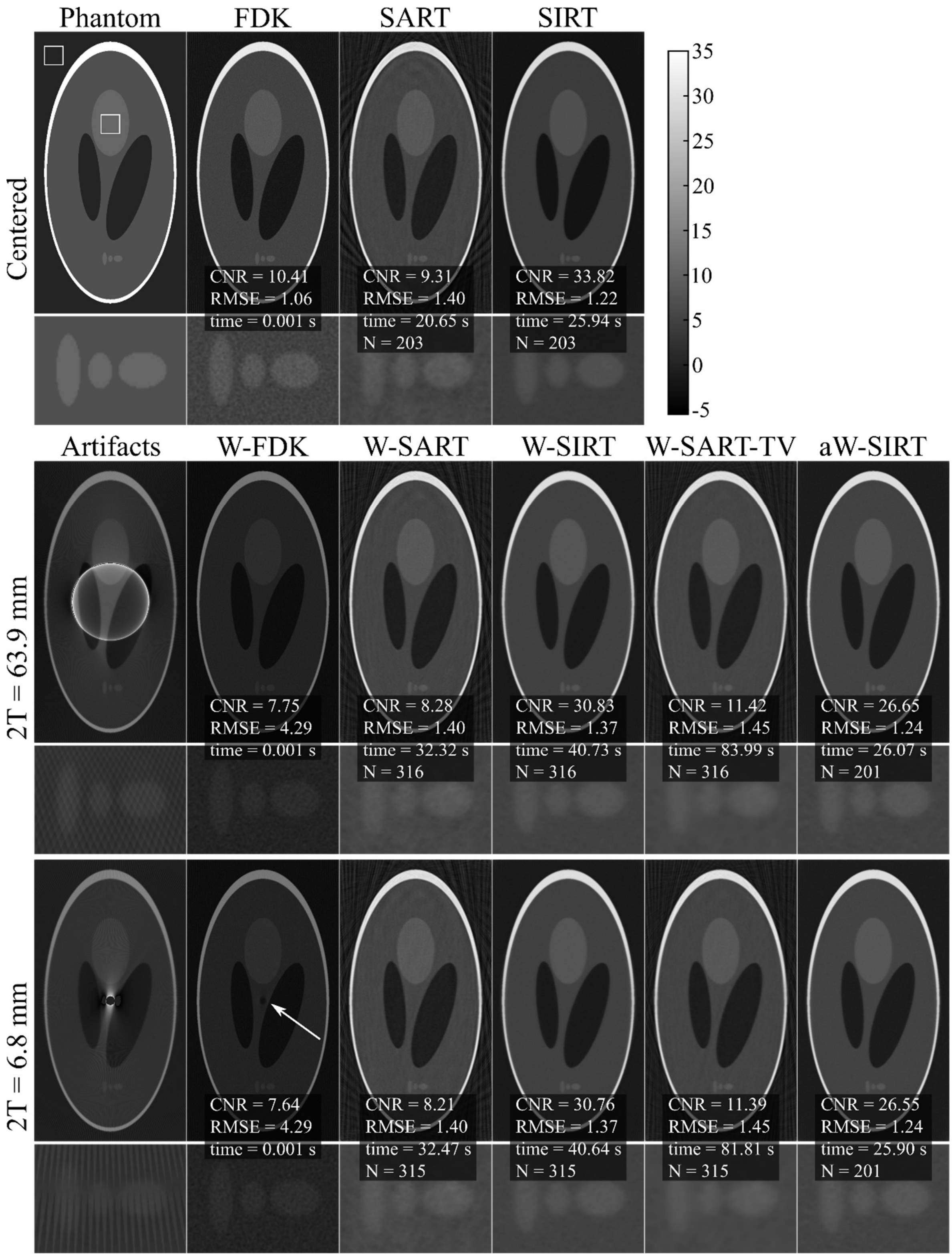

Figure 5: Central slice reconstructions using the different reconstruction methods under consideration (different columns) for a centered detecter (first row), an overlap region of $2T = 63.9$ mm (second row), and an overlap region of $2T = 6.8$ mm (bottom row). The first column shows the phantom and typical artifacts that occur when no weighting is applied in an offset geometry. On the original phantom, two white squares of equal size indicate the regions used for CNR calculations. On each panel, the CNR, RMSE with the original phantom slice, total reconstruction time and number of iterations are indicated. Below each panel, an ROI if the three elliptic shapes in the bottom of the slice are shown to highlight details. The white arrow in the bottom row indicates remaining artifacts when using pre-convolutional FDK for small overlap sizes. The grayscale in the top left applies to all panels.

may also introduce streak artifacts outside of the overlap region. It is shown that all of the proposed weighted reconstruction methods successfully remove the artifacts. The only exception is the pre-convolutional FDK method in case of a small detector overlap, where an artifact remains in the center (white arrow in bottom row). This was expected, as it was already shown in early literature that pre-convolutional FDK introduces artifacts in the case of a small redundancy region (Cho *et al* 1996).

It is shown that, in the case of a centered detector, the FDK algorithm provides the best reconstruction in terms of RMSE and speed, but the SIRT algorithm provides the best CNR. The SART reconstruction displays some non-uniformity (mostly in the background) and has a CNR comparable to the FDK reconstruction, but it is faster than the SIRT algorithm for the same number of iterations. When the detector is laterally shifted, the CNR drops and the RMSE rises for the W-FDK method. The rise of RMSE is due to the fact that the raw output of the FDK algorithm is globally darker than the original phantom, which is not the case for the iterative methods. The SART methods provide a higher CNR and a lower RMSE than FDK, showing that the SART methods can deliver better reconstructions at the cost of a longer computation time, which is most apparent using the W-SART-TV method. The TV denoising step results in a better CNR, but a slightly lower RMSE at the cost of a steep increase of the computation time. The W–SIRT method is slightly slower than the W-SART method, but the CNR is vastly increased and the RMSE is slightly lower. The aW-SIRT method is the fastest of the proposed weighting schemes and provides an RMSE which approximates the RMSE of a centered SIRT reconstruction, at the cost of a slightly lower CNR as compared to the W-SIRT algorithm. For the iterative methods, the CNR and RMSE seem to be unaffected by the amount of detector overlap.

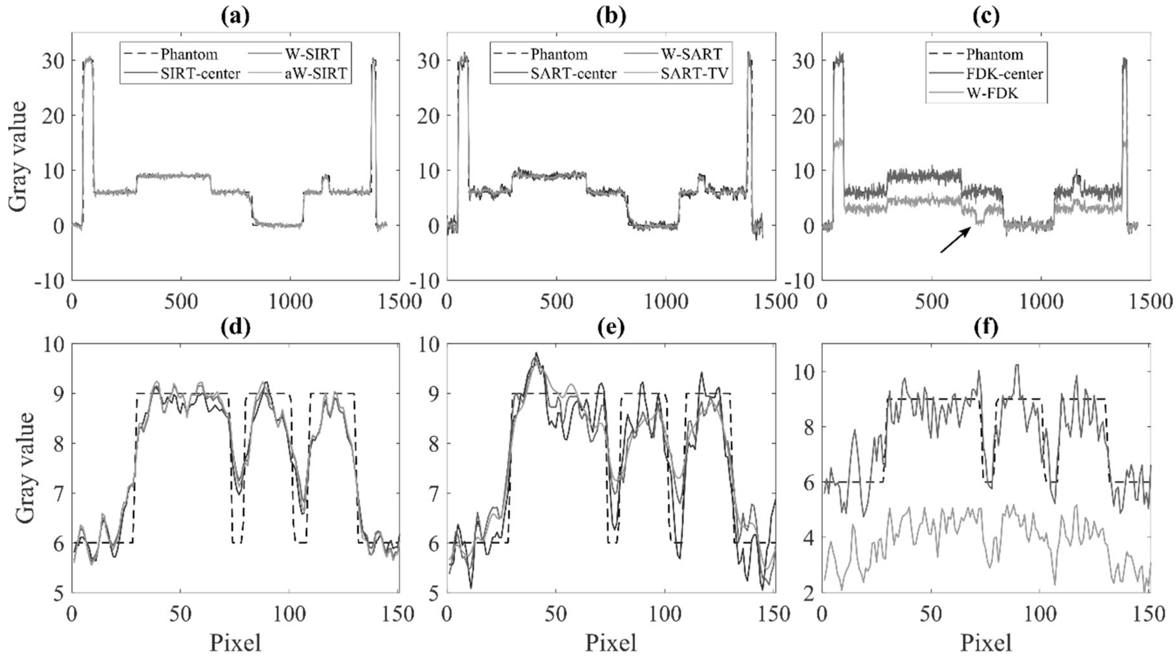

Figure 6: Vertical cross-sections at the center of the reconstructed central slice for **(a)** the SIRT methods, **(b)** the SART methods, and **(c)** the FDK methods. Panels **(d)**-**(f)** show horizontal cross-sections through the center of the three elliptical shapes at the bottom of the slice in the same order. The black arrow in panel **(c)** highlights the redundancy artifact that remained using FDK for a small redundancy region. The legends in the top panels also apply to the corresponding panels below.

Visually, both the SIRT and SART methods provide decent reconstructions, but the SIRT methods seem to suffer less from noise, as is also shown in figure 6. This figure shows line profiles of vertical cross-sections at the center of the reconstructed slices (panels **(a)-(c)**) and horizontal cross-sections through the center of the three elliptic shapes at the bottom of the slices (panels **(d)-(f)**). For the weighted reconstructions, only the line profiles of the reconstructions for which $2T = 6.8$ mm are shown, as the curves are nearly identical to those of $2T = 63.9$ mm. By comparing panels **(a)** to **(c)**, it is clear that the SIRT reconstructions are superior in terms of noise suppression, followed by the SART reconstructions. For the weighted FDK method, it is shown that the gray values lie substantially lower than those of the original phantom and centered reconstruction. From the line profiles, it seems that the gray values are roughly half of what they ought to be. Also, the dip in the gray values caused by the unsuccessful removal of the central artifact is visible, as indicated using a black arrow. In panels **(a)** and **(b)** it is hard to discriminate between the line profiles of the different methods, but differences are more noticeable in panels **(d)** and **(e)**, although the line profiles for the three SIRT methods show no considerable differences. The line profiles in panel **(e)** show that the W-SIRT-TV method indeed reduces the noise, resulting in an increase of CNR. In panel **(f)** it is again shown that the weighted FDK results in overall lower gray values, and the three peaks of the elliptical shapes are nearly unidentifiable due to the noise.

3.2 LEGO test phantom

As formerly described, the detector was manually shifted over distances of approximately 25 mm. Subsequent to each lateral shift, a calibration dataset, as well as a dataset of the LEGO phantom, was recorded. After calibration, the different detector shifts were found to be $\Delta = \{26.6,\ 45.5,\ 63.5,\ 89.7\}$ mm. For each of the lateral shift values, the datasets were reconstructed using W-SART, W-SIRT, and aW-SIRT in a reconstruction volume of 650 voxels × 500 voxels × 800 voxels with a voxel size of 285 mm. The convergence rates of the different methods were examined first.

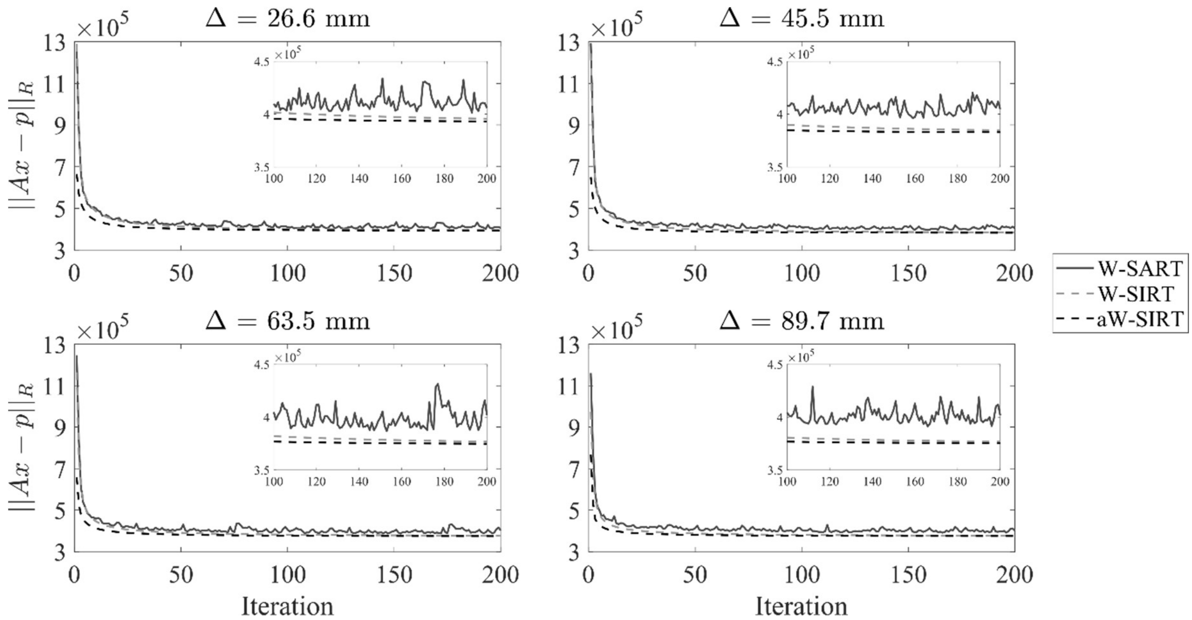

Figure 7: Convergence curves for each of the values for the lateral detector shifts $\Delta = \{26.6,\ 45.5,\ 63.5,\ 89.7\}$ mm and the different reconstruction methods. In each panel, the inset shows the RN values for the last 100 iterations to increase the visibility of the difference between the curves. The legend applies to all panels.

Figure 7 shows that, as predicted by the simulations, the aW-SIRT algorithm has a faster convergence rate as compared to W-SIRT due to the relaxation parameter. The convergence curves of W-SIRT and W-SART are quite similar during the first few iterations, but it is clear that later on, the W-SIRT algorithm converges more stably. While the W-SIRT algorithm converges to the same value for the RN as aW-SIRT (only slower) after about 200 iterations, the same is not true for the W-SART algorithm, as seen in the insets. The similarity of the curves in the different panels indicates that the convergence rates of the methods are not affected by the amount of lateral detector shift.

Next, figure 8 shows horizontal reconstructed slices of the LEGO phantom of different heights (h_1 = - 9.98 mm, h_2 = 8.85 mm, and h_3 = 27.95 mm relative to the center of the reconstructed volume) for a centered reconstruction using 200 iterations of SIRT and for reconstructions obtained using a shifted detector (Δ =89.7 mm) using 200 iterations of W-SART, W-SIRT and aW-SIRT. Slices for other values of the detector shift are not shown as they appear nearly identical. It is observed through visual inspection that for the shifted reconstructions, no circular artifact is present coaxial to the rotation axis, which implies that the weighting scheme indeed corrects for data redundancy and edge truncation in the reconstruction algorithms under consideration. By comparing the edges of the LEGO bricks close to the center of the volume to those closer to the edge of the object, it is seen that the edges away from the center become more blurry. This is rotation blur caused by recording projections under continuous rotation and is unrelated to the proposed reconstruction algorithm or weighting scheme. The ROI's shown below each panel indicate that in general, the reconstruction obtained with W-SIRT is slightly more blurry than the one obtained with W-SART, but it is also less noisy. The reconstruction obtained with aW-SIRT seems sharper than those obtained with W-SART and W-SIRT, but appears to be noisier than the W-SIRT reconstruction. To quantitatively assess the contrast in the different reconstructed volumes, the CNR was calculated in the three gear-shaped objects

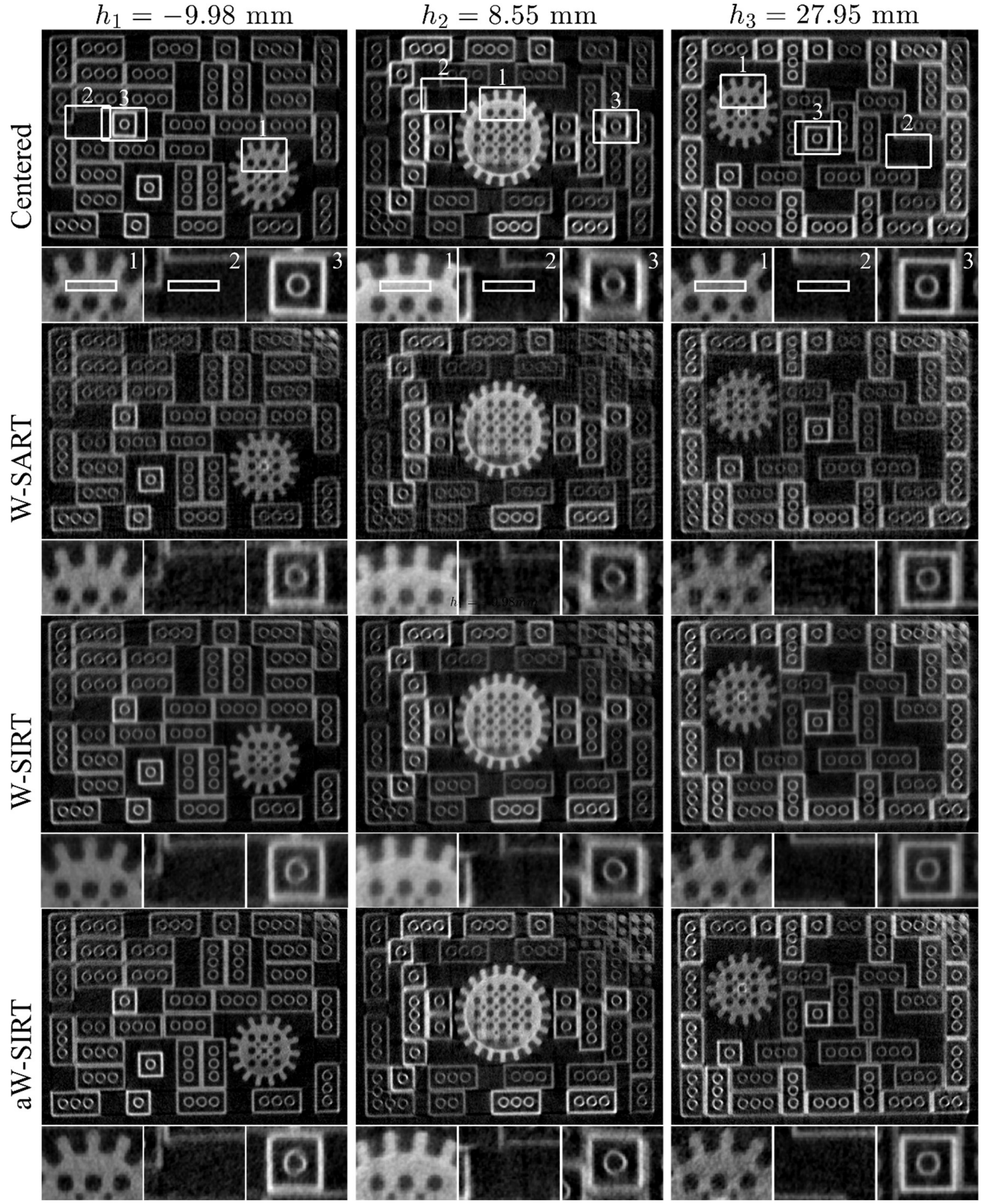

Figure 8: Horizontal reconstructed slices of the LEGO phantom at heights h_1 = -9.98 mm (left column), h_2 = 8.85 mm (middle column), and h_3 = 27.95 mm (right column) relative to the center of the reconstructed volume for each of the reconstruction algorithms under consideration (centered SIRT, W-SART, W-SIRT, and aW-SIRT). Below each full panel, ROI's are shown that are indicated in the top row using white rectangles and numbers 1 to 3. ROIs 1 and 2 contain white rectangles of 10 pixels × 50 pixels to indicate the image regions used for CNR calculations. The gray values in all panels are windowed between 0 and 40.

that are located on the three different heights (h_1, h_2, and h_3). In ROI 1 and ROI 2 of the first row, white rectangles of 10 voxels × 50 voxels indicate the regions that were used for CNR calculations. The calculations were performed for each of the reconstruction algorithms and each value for detector shift, as well for the centered reconstruction (using 200 iterations of regular SIRT). In table 4, the results of the CNR calculations are shown, along with information on the computation times of the algorithms and the total effective FOV obtained by applying the lateral detector shift, which is calculated as the sum of the true width of the detector d and twice the shift value Δ. Apart from the CNR, also the RMS contrast, calculated over the full reconstructed volume using equation (6), is shown. In the table, the same results are shown for 100 iterations.

Table 4: Experimental results using the LEGO phantom

N_{it}	Δ (mm)	FOV (mm)	method	CNR_1	CNR_2	CNR_3	$\langle CNR \rangle$	C_{RMS}	Δt (s)
	0	292.0	SIRT	17.88	16.76	12.56	15.74	8.35	1814.7
			W-SART	12.11	13.33	6.44	10.63	7.48	1437.7
	26.6	345.2	W-SIRT	19.82	15.92	15.37	17.04	7.12	2260.1
			aW-SIRT	13.56	13.42	9.77	12.25	7.94	2075.6
			W-SART	12.94	18.91	8.85	13.57	7.27	1658.5
	45.5	383.0	W-SIRT	21.53	25.41	14.88	20.61	6.98	1990.2
200			aW-SIRT	13.71	20.30	10.21	14.74	7.78	1990.6
			W-SART	14.24	15.38	10.14	13.25	7.32	1730.7
	63.5	419.0	W-SIRT	21.48	19.39	20.90	20.59	7.09	1967.6
			aW-SIRT	14.01	15.43	13.08	14.17	7.87	1974.3
			W-SART	9.96	14.30	9.30	11.18	7.32	1883.8
	89.7	471.4	W-SIRT	15.29	19.83	19.25	18.13	7.20	1923.8
			aW-SIRT	10.77	14.77	12.26	12.60	7.93	1956.0
	0	292.0	SIRT	27.20	21.11	19.17	22.49	7.55	1493.0
			W-SART	13.40	16.52	9.47	13.13	6.63	1196.0
	26.6	345.2	W-SIRT	24.82	20.18	22.88	22.62	6.27	1658.9
			aW-SIRT	19.86	15.93	15.41	17.07	7.12	1661.1
			W-SART	15.26	25.72	10.21	17.06	6.43	1209.7
	45.5	383.0	W-SIRT	34.37	33.83	20.96	29.72	6.14	1620.8
100			aW-SIRT	21.59	25.43	14.92	20.65	6.98	1621.4
			W-SART	16.87	18.62	13.21	16.23	6.49	1218.6
	63.5	419.0	W-SIRT	35.27	25.83	33.92	31.67	6.25	1583.4
			aW-SIRT	21.54	19.41	20.97	20.64	7.09	1583.5
			W-SART	12.49	17.44	13.33	14.41	6.51	1247.7
	89.7	471.4	W-SIRT	22.59	27.57	29.67	26.61	6.37	1523.7
			aW-SIRT	15.31	19.86	19.31	18.16	7.19	1548.7

For each value of lateral detector shift Δ (and corresponding effective detector width d_{eff}), the value of the CNRs is shown along with the total reconstruction time. CNR_i corresponds to the CNR calculated in the slice at h_i, and the average CNR over the different heights is given as $\langle CNR \rangle$. The value of C_{RMS} is calculated over the full reconstructed volume. The number of iterations is given by N_{it}.

Table 4 shows that, in general, the average CNR is decreased when an offset geometry is used. This is probably caused by the detector recording less rays that pass through the object and more background rays (in the case of the LEGO phantom), resulting in less recorded signal, which would increase the noise. However, this does not hold for the W-SIRT method, as the CNR appears to be higher as compared to the centered reconstruction for the same number of iterations. This is understood by considering that the W-SIRT algorithm converges slower than the centered SIRT algorithm and thus the fine details, such as noise, are only reconstructed in later iterations. Therefore, the W-SIRT is expected to produce more homogeneous regions in the signal and the background, resulting in a higher CNR. This does not mean that the contrast itself is better (see figure 9). By comparing the average CNR values of W-SART, W-SIRT, and aW-SIRT, those of W-SART are found to be lower than those of W-SIRT and aW-SIRT, probably because SART is inherently more sensitive to noise (see convergence curves). Based on the obtained values for the C_{RMS}, there is a loss of contrast when the detector is shifted laterally for the same number of iterations, regardless of the reconstruction method used. However, the contrast in the aW-SIRT reconstructions is the greatest, followed by W-SART and W-SIRT for the same number of iterations. It is also noticed that the CNR and C_{RMS} values for the W-SIRT reconstructions using 200 iterations are very similar to those of the aW-SIRT reconstructions using only 100 iterations, regardless of the detector shift. This may imply that the application of the relaxation parameter approximately doubles the convergence rate. The reconstruction times of W-SART are generally shorter than those of W-SIRT and aW-SIRT, but seem to increase with increasing detector shift. This is understood by the fact that W-SART, in contrast to W-SIRT and aW-SIRT, requires the projection data to be padded with zeros outside the redundancy region where data is non-existent. This implies that the size of the projection data grows in size as the detector shift is increased, resulting in the rise of memory usage. The W-SART method was also applied without padding the projection data, but this resulted in uncorrected redundancy artifacts (not shown in this work), while W-SIRT and aW-SIRT also produce redundancy-artifact-free reconstruction without data padding. The reconstruction times of W-SIRT and aW-SIRT are similar, but seem to slightly decrease by increasing the detector shift. This is quite remarkable, as the only difference between the datasets are the gray values of the projection data and the values in the matrix $\boldsymbol{W}$. A possible explanation for this is the fact that, for a larger detector offset, the projection data contains more background pixels, which can assume the value of zero, and the matrix $\boldsymbol{W}$ contains more values that are equal to one instead of decimal numbers between zero and one. This might be more efficient in the calculations involved, although we do not claim this is the reason why.

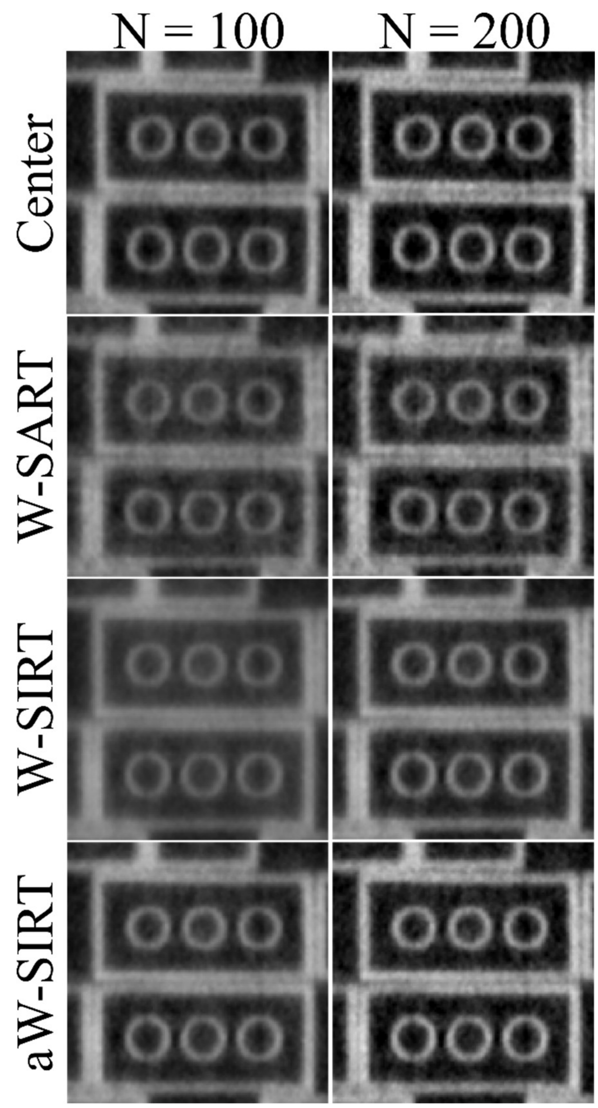

Figure 9: Central regions of slices at h_1 and $\Delta = 26.6$ mm using 100 and 200 iterations of centered SIRT, W-SART, W-SIRT, and aW-SIRT. The gray values are windowed between 0 and 30.

Figure 9 shows central regions of the reconstructed slice at h_1 with $\Delta = 26.6$ mm for a centered reconstruction using 100 or 200 iterations of SIRT and shifted reconstructions using 100 or 200 iterations of W-SART, W-SIRT, and aW-SIRT. Comparing the regions for the same number of iterations shows that, visually, the W-SART and W-SIRT algorithms produce slices with decreased contrast (mostly W-SIRT), but the W-SART reconstruction seems noisier. The slices reconstructed using aW-SIRT visually resemble the slices of the centered detector the most and therefore may be more favorable. The visual quality of the centered reconstruction for 100 iterations is very similar to the W-SIRT and aW-SIRT iterations using 200 and 100 iterations, respectively. These visual observations are in agreement with the CNR and C_{RMS} values reported in table 4.

3.3 Large objects

After validation of the proposed method on the LEGO phantom (which was sufficiently small to be imaged with a centered detector), the method was tested on two samples for which the detector offset method is required. The first large sample is the PMMA container with PVC tubes, the second is the frozen rabbit specimen (see figures 3**(b)** and 3**(c)**). The phantom containing PVC tubes in a PMMA case was imaged twice: the first time it was empty (or filled with air) and the second time it was filled with water. The lateral shift of the detector was equal to 111.9 mm according to the calibration, yielding an effective FOV of 515.8 mm, which is a gain of 76.6% compared to the FOV of the centered detector (292 mm). The phantom was reconstructed in a volume of 800 voxels × 800 voxels × 1450 voxels with a voxel size of 0.285 mm. Figure 10**(a)** shows the convergence curves for the reconstruction of the PMMA phantom in an empty state. The curves for the water-filled PMMa phantom are not shown as they are very similar. As is the case for the LEGO phantom, the aW-SIRT algorithm has the fastest convergence rate, and the curve of the W-SART algorithm is more unstable.

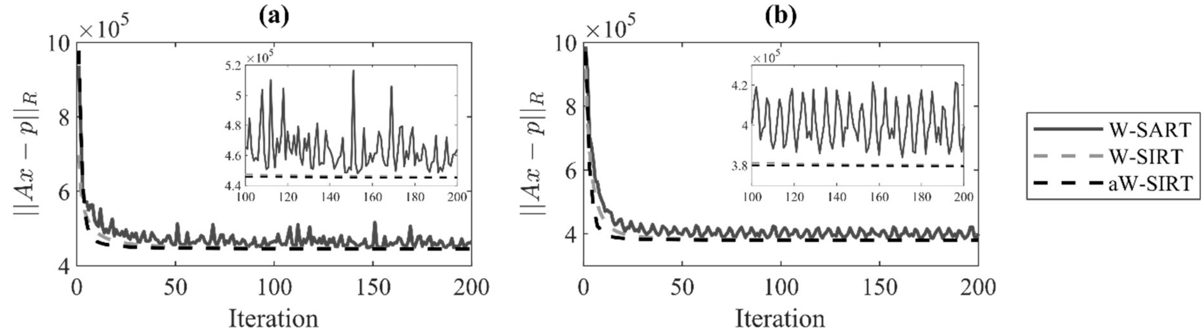

Figure 10: Convergence curves of **(a)** the empty PMMA phantom and **(b)** the rabbit specimen for 200 iterations. The convergence curves of the water-filled PMMA phantom are not shown as the curves are very similar. In both panels, the inset shows the curves for the last 100 iterations to highlight differences between the methods.

Horizontal (view along the rotation axis) and vertical (view perpendicular to the rotation axis) slices of the reconstructed phantom are shown in figure 11. As the LEGO phantom experiments showed that the reconstructions using 200 iterations of W-SIRT and 100 iterations of aW-SIRT were nearly identical, only slices of 100 iterations of aW-SIRT are shown. The number of iterations of the W-SART reconstruction was 200. In the left column, artifacts related to positioning the detector in an offset position can be clearly seen, as no redundancy weighting was applied. These artifacts are observed in the form of a bright circular artifact coaxial to the rotation axis, causing additional shading artifacts as well (mostly observed in the lower two panels of the left column). Using W-SART or aW-SIRT, these artifacts are successfully removed. Visual inspection of the slices suggests that the slices obtained using aW-SIRT are slightly less noisy. Quantitative measures such as CNR and C_{RMS} can be found in table 5.

In figure 11, it is important to notice that in the bottom row, when the phantom is filled with water, the contrast for the long tube disappears near the center of the volume. This is not the case when the phantom is filled with air (second row). The disappearance of this contrast is thus not related to positioning the detector in an offset position but is due to the limited dynamic range of the XRII. The shorter tubes suffer less from this contrast loss, showing that shapes of large aspect ratio are more sensitive to this artifact. As animals, for example, usually have such aspect ratio, these artifacts are important to consider. Nevertheless, this experiment proves the possibility of reconstructing an object of which the width exceeds the width of the detector by positioning the detector in an offset position and by using the aW-SIRT algorithm.

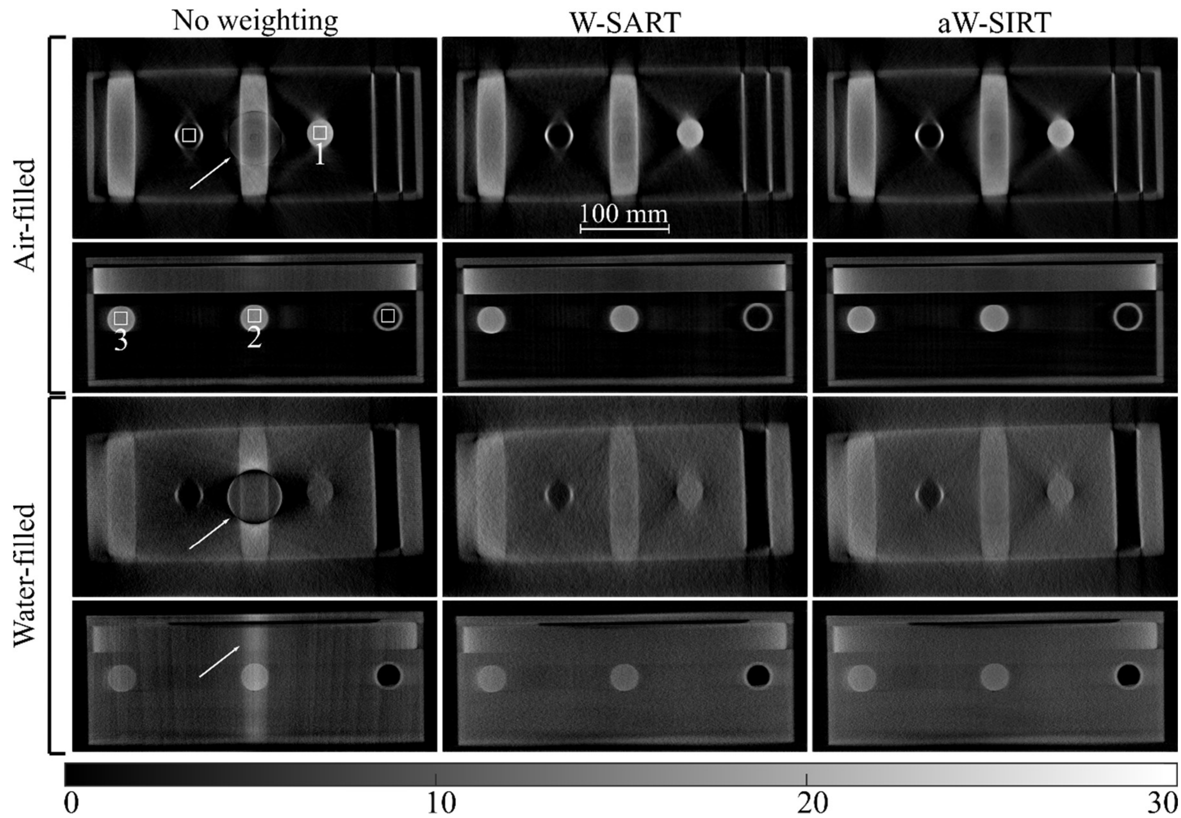

Figure 11: Reconstructed slices of the PVC tube phantom filled with air (top two rows) and filled with water (bottom two rows) obtained using 100 iterations regular SIRT without applying redundancy weighting (first column), using 200 iterations W-SART (second column), and using 100 iterations aW-SIRT (last column). The first and third row shows horizontal slices, whereas the second and fourth row shows vertical slices. White arrows on the slices in the left column indicate artifacts and the white squares of 50 voxels × 50 voxels indicate the regions that were used for CNR calculations (the regions in the signal are labeled using the number 1 to 3). The scale bar in the top middle panel and the grayscale below apply to all panels.

Table 5 shows that, in case the phantom is empty, the aW-SIRT provides a reconstruction with higher CNR as compared to W-SART. When the phantom is filled with water, the differences are smaller. The differences in C_{RMS} are not in favor of one method. It is, however, important to notice that the results obtained using aW-SIRT only required 100 iterations at a time of ~ 4800 s, while W-SART required 200 iterations and a total computation time of $\sim 8400\ s$. As the CNR and C_{RMS} do not differ much, the best choice would in this case be the aW-SIRT algorithm due to the (much) shorter computation time.

Table 5: Experimental results using the PMMA phantom

Δ (mm)	FOV (mm)		Method	N_{it}	CNR_1	CNR_2	CNR_3	$\langle CNR \rangle$	C_{RMS}	Δt (s)
111.9	515.8	E	W-SART	200	29.78	22.27	23.82	25.29	3.54	8371.9
			aW-SIRT	100	30.32	26.53	27.84	28.23	3.57	4761.6
		W	W-SART	200	8.17	13.63	16.31	12.70	3.76	8357.3
			aW-SIRT	100	9.44	12.88	15.36	12.56	3.85	4734.3

In this table, the letters E and W indicate whether the PMMA phantom is empty (or air-filled) or water-filled, respectively. The different CNR values correspond to the labeled regions in figure 11. Same symbols as in table 4 apply.

Finally, to demonstrate our proposed method on a biological sample, a rabbit specimen was scanned with parameters that can be found in table 2. During this experiment, the detector was shifted over $\Delta = 110$ mm, yielding a redundancy region of $2T = 72$ mm and an effective FOV of 512 mm. The reconstructed volume had a size of 1200 voxels × 500 voxels × 1450 voxels with a voxel size of 285 mm. Convergence curves of the different algorithms can be found in figure 10**(b)**. Again, the aW-SIRT algorithm is found to converge at the fastest rate, while the convergence curve of the W-SART algorithm displays instability. In figure 12, ROI's of vertical slices (parallel to the rotation axis) of the rabbit are shown, displaying the pelvis, the spine and ribs, and the head and teeth. The slices were obtained using 200 iterations of W-SART and 100 iterations of aW-SIRT. As the experiments with the PMMA phantom already showed that both methods would remove the redundancy artifacts, slices of a non-weighted reconstruction are not shown. Visual inspection of the slices suggests that the slices of the aW-SIRT reconstruction are slightly less noisy (mostly visible in the slice containing the pelvis). The slice containing the spine and ribs displays a slightly better contrast in the aW-SIRT reconstruction. The teeth seem to be more distinguishable in the aW-reconstruction, and the edge at the mouth of the rabbit seems sharper. Some ring artifacts are still visible when using the W-SART or aW-SIRT method, which are visible as subtle black vertical streak in the slice showing the pelvis. These originated from remaining dark-field artifacts and are unrelated to the proposed method. For these reconstructions, three values for the CNR were calculated in the soft tissue (see white squares in the top row of figure 12) and the C_{RMS} values for the total volumes were calculated and reported in table 6:

Table 6: Experimental results obtained using the rabbit specimen

Δ (mm)	FOV (mm)	Method	N_{it}	CNR_1	CNR_2	CNR_3	$\langle CNR \rangle$	C_{RMS}	Δt (s)
110	512	W-SART	200	23.40	27.25	27.32	29.79	4.14	7621.2
		aW-SIRT	100	29.97	29.24	30.14	25.99	4.17	4414.8

The index of the CNRs reported in this table corresponds to the number of the column in figure 12. Same symbols as in table 5 apply.

Table 6 shows that in general, the CNR values for the aW-SIRT reconstruction are higher, which is in agreement with the visual inspection. However, the difference in C_{RMS} is negligible. Again, only 100 iterations of the aW-SIRT algorithm were used to obtain these results, yielding a shorter total computation time as compared toW-SART.

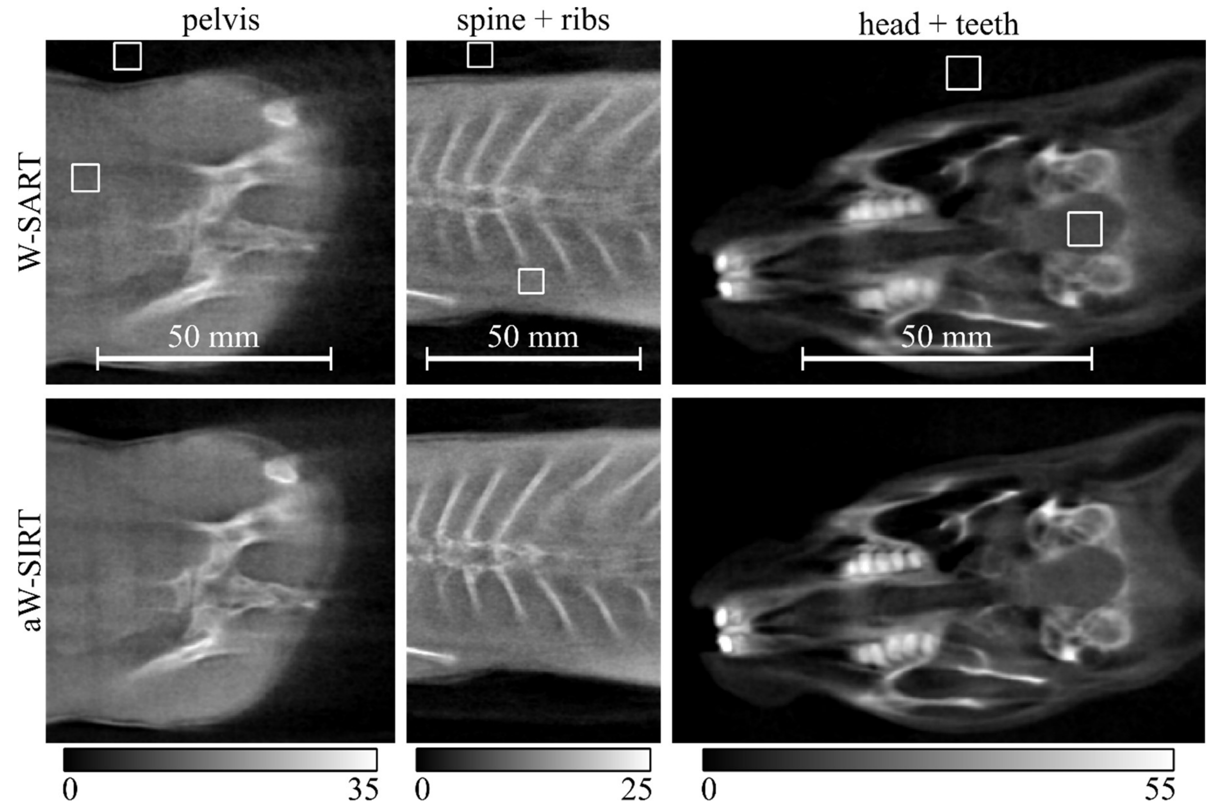

Figure 12: Vertical slices showing different anatomical structures of the rabbit specimen, namely the pelvis (left column), the spine and the ribs (middle column), and the head and the teeth (right column). The top row shows the slices obtained with 200 iterations of W-SART, whereas the bottom row shows those obtained using 100 iteration aW-SIRT. In the top row, the white squares (20 voxels × 20 voxels) indicate regions in the tissue and the background that were used for CNR calculations. The grayscale and 50 mm scales apply to their corresponding column.

As one of the goals of this work is to propose a method to increase the field of view for tomographic reconstruction, we demonstrate the field-of-view gain in the extended reconstructed volumes, by providing images of 3D renderings of the rabbit and the PMMA phantom (empty and water-filled) using maximum intensity projection. The images can be found in figure 13.

(a) (b) (c)

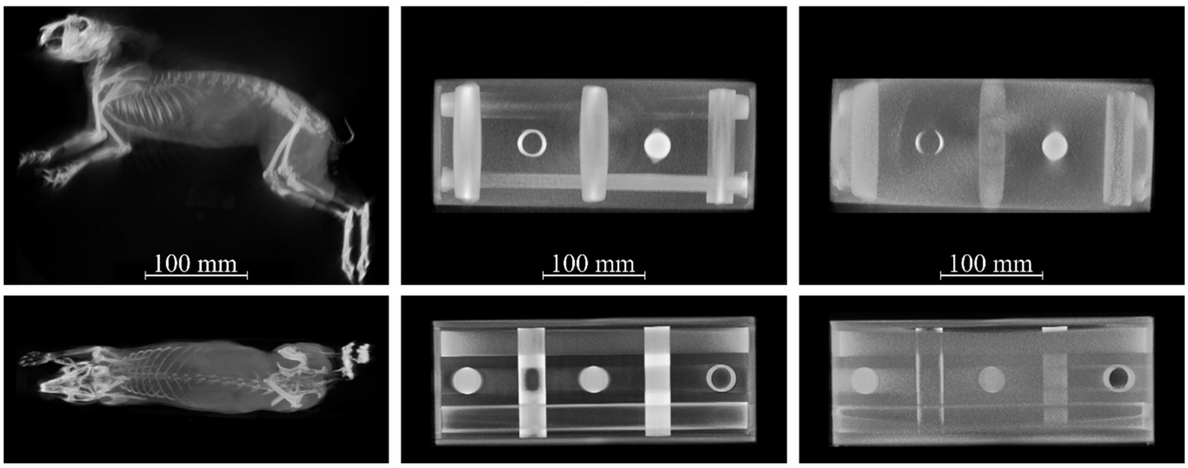

Figure 13: Side and top views (top and bottom row) of 3D-renderings using maximum intensity projection. **(a)** Rabbit specimen. **(b)** Empty PVC tube phantom. **(c)** Water-filled PVC tube phantom.

4. Discussion

The proposed redundancy weighting scheme implemented in the SIRT algorithm (W-SIRT) was first tested in simulations using central slice reconstructions of 3D Shepp-Logan phantom. It was compared to the pre-convolutional FDK method and the W-SART(-TV) method. The convergence curves (figure 4) readily showed that, by positioning the detector off center and by applying the redundancy weighting scheme, the convergence rate decreased. This was both true for SIRT and SART. A decrease of convergence rate is an undesirable side-effect of the method, and would imply that more iterations are needed to obtain a converged reconstruction. To this end, we introduced a relaxation parameter α in the W-SIRT scheme, resulting in the aW-SIRT algorithm. Following the work of Gregor and Benson, the relaxation parameter α was chosen as 1.99. This turned out to be a reasonable choice, as indeed the convergence rate was increased and the convergence curve of a centered detector was approximated. Whether the convergence rate of the aW-SIRT algorithm can be accelerated even further is yet to be studied. Presumably, higher convergence rates can be achieved by using other SIRT-like methods, such as the Conjugate Gradient Least Squares (CGLS) method or a Barzilai-Borwein approach. However, this is beyond the scope of the current work.

Another important result obtained from the simulations is that the weighted SIRT and SART algorithms perform well for both small and large detector shifts (Hansis *et al* 2010, Bian *et al* 2012), which is not the case for pre-convolutional FDK. However, the W-SIRT and aW-SIRT algorithm seem to provide reconstructions with a higher CNR and lower RMSE as compared to SART and SART-TV. Due to the high convergence rate of the aW-SIRT algorithm, less iterations are necessary to reach convergence, resulting in a lower total computation time than W-SART, although the average computation time per iteration is shorter for W-SART. The benefits of incorporating TV denoising in the W-SART algorithm are limited, and the vast increase in computation time deteriorates its usefulness for reconstructing large 3D volumes. Finally, we highlight the fact that, in the simulations, the detector used was of the flat-panel type. This indicates that the proposed method applies to flat-panel detectors as well, requiring no alterations, demonstrating the generality of the method.

After conducting simulations, we have tested our proposed method using experimentally using different study objects, each with their own purpose. Using the LEGO phantom, the convergence rate, image quality (in terms of CNR and C_{RMS}), and computation time were assessed for the different reconstruction algorithms and for the different values of detector offset. It was shown that the aW-SIRT algorithm indeed has the fastest convergence rate due to the relaxation parameter, and that the convergence of W-SIRT and aW-SIRT is more stable as compared to W-SART. This implies, as shown in table 4, that desired levels of CNR and C_{RMS} can be reached faster using aW-SIRT as opposed to W-SIRT or W-SART. Given the larger values for the CNR and the C_{RMS} of the aW-SIRT algorithm as compared to the W-SART algorithm, it might be possible to obtain reconstructions with the aW-SIRT algorithm of the same image quality as those obtained with W-SART, but with a lower dose. The methods were not compared to FDK in the experiments due to the complex imaging geometry, but the simulations also pointed out that higher CNRs could be obtained using iterative methods instead of FDK. The data in table 4 and the ROIs shown in figure 9 are in favor of the aW-SIRT algorithm, provided that the number of iterations is limited. For example, 100 iterations of the aW-SIRT algorithm were sufficient to obtain a reconstruction of similar quality using 200 reconstructions of W-SIRT, while the visual quality was similar to that of a centered reconstruction using 100 iterations of SIRT.

The general loss of CNR in the reconstructed slices using detector offset geometry was reported earlier by Mettivier *et al.* in a phantom study in the field of breast CBCT (Mettivier *et al* 2012). However, it was also shown in their work that by blocking the fraction of the beam that would irradiate the sample but would not be seen by the detector (due to the offset position) before it reaches the sample, the amount of scatter and the dose would decrease. This resulted in a larger contrast-to-noise ratio per unit dose (CNRD) as compared to a centered detector. Collimation of the 'unuseful' part of the beam was not applied in this work, but the combination of this half-beam collimation in combination with aW-SIRT reconstruction yields interesting opportunities for dose reduction at fixed image quality. This is, however, beyond the scope of the current work.

As seen in figure 9, the reconstructed slices of the LEGO phantom exhibited blurring artifacts near the periphery of the reconstructed volume. These artifacts are unrelated to the detector offset method as these were also present in the case of a centered detector. Presumably, these artifacts are caused by continuously rotating the sample while recording. In other experiments (not described in this manuscript) we have enlarged the rotation period while decreasing the shutter time to eliminate the angular integration, as described by Krebs et al. (Krebs *et al* 2018), but the artifacts remain. We therefore believe that the blurring artifacts might be due to scintillator lag, as XRIIs are known to have lag times of the order of milliseconds (Wang and Blackburn 2000). As larger objects (which are the aim of FOV enlargement techniques) will suffer more from these blurring artifacts, it is an important aspect to consider in offset detector applications.

Using the PMMA phantom, the W-SART and aW-SIRT algorithms proved to be able to reconstruct large objects free of artifacts related to positing the detector in an offset position. When the phantom was filled with water, it was observed that the contrast between the long PVC tube and the water completely disappeared in the center region of the volume. This did not occur in the shorter tubes, so it is clear that larger, more elongated (high aspect ratio) structures will suffer more from contrast loss. The quantitative results shown in table 5 were slightly more in favor of the aW-SIRT algorithm for the empty phantom, but the differences were less pronounced when the phantom was filled. However, the shorter computation time of the aW-SIRT is a great advantage.

The reconstructed slices of the rabbit using W-SART and aW-SIRT were free of redundancy-related artifacts. However, by inspecting the grayscales of figure 12, it can be noticed that the grayscale in the middle column has the smallest window. This implies that there is less overall contrast in that region as compared to the slice of the head (much larger window). This loss of contrast is again due to the limited dynamic range of the system, as was also the cause for the loss of contrast in the long PVC tube. The reported values of CNR and computation time, as well as the visual quality, are in favor of the aW-SIRT method. Nearly identical results were obtained using 200 iterations of W-SIRT, but the computation time would then nearly double and exceed the computation time of W-SART. It is therefore strongly advised to build in a relaxation parameter when using a weighted SIRT approach.

Using the aW-SIRT (or W-SIRT) algorithm, we have shown that the effective FOV of the detector could be increased by 75% (see results of PMMA and rabbit sample), which is a considerable gain. In theory, the effective detector width could be increased even further, but since our system is highly modular and depends on phantom-based calibration (Nguyen *et al* 2021), the extension of the field-of-view is experimentally limited. The beads in the calibration phantom should be visible in each frame, so the size of the overlap region should be large enough to contain the full phantom. Furthermore, such a flexible set-up with large components placed on trolleys and ceiling gantries is modified by hand and can, therefore, only be aligned and repositioned with limited accuracy.

The work presented in this paper can, for example, be of interest to researchers in the field of small animal biomechanics using stereoscopic x-ray systems. These systems provide information on animal movement, but morphological data of the specimen (such as bone segmentation) needs to be gathered in a separate CT-system, which is rarely available in the same facility. In this work, not only do we prove that such systems can be extended to tomographic systems by introducing a rotation stage, but the size of the reconstruction volume can be also enlarged to measure the size of the animal to be imaged. This, for example, paves the way for longitudinal studies of young animal development, because locomotion data, as well as morphological data, can be gathered in the same set-up, circumventing the issue of animal transportation between facilities. The effective FOV (and thus the diameter of the reconstruction volume) can be enlarged to a certain extent during the growth period of the animal under consideration. However, we pointed out that continuous rotation of the sample and the limited dynamic range might pose issues while imaging larger animals of high aspect ratio in such a system. This is of course one of the fields that could benefit from this work, as the implementation of the W-SIRT and aW-SIRT algorithms are not field-specific.

It leaves us to mention that the proposed W-SIRT and aW-SIRT methods are convenient to implement using the ASTRA toolbox, given the fact that both methods are nearly purely matrix multiplications, except for the creation of matrices $\boldsymbol{A}$, $\boldsymbol{R}$, $\boldsymbol{C}$, and $\boldsymbol{W}$. For large-scale datasets, the matrix $\boldsymbol{A}$ is too large to store explicitly, and therefore, implementations based on explicit matrix computations (as in MATLAB) cannot be used for (for example) the SIRT algorithm. However, an interface was developed in the ASTRA toolbox (Bleichrodt *et al* 2016) that makes use of the Spot toolbox, which allows wrapping external, GPU-based codes for linear operations in MATLAB objects that can be treated as matrices (van den Bergh and Friedlander 2013). This implies that the linear operations of the forward and backward projection can be defined and treated as matrices in the MATLAB interface, allowing for an intuitive implementation of the SIRT algorithm. Instructions on how to implement the SIRT algorithm using the ASTRA opTomo operator can be found in the work of Bleichrodt *et al.* and can be extended to the W-SIRT or aW-SIRT algorithm by incorporating the redundancy weighting matrix W and relaxation parameter α.

5. Conclusion

In this work, we have presented the implementation of redundancy weighting in the well-known SIRT algorithm for detector offset tomography. The proposed algorithms were validated in both simulations and experiments, where it was shown that artifacts in the reconstructions related to placing the detector in a non-centered position were successfully removed. To use the algorithm in a useful way, we have proven that the inclusion of an additional relaxation parameter will accelerate the convergence. Using a relaxation parameter, higher CNR values could be obtained as compared to a weighted SART approach, at a much shorter computation time. As opposed to pre-convolutional FDK, the aW-SIRT algorithm performs well for both small and large detector shifts, resulting in a maximum increase of the width of the reconstructed volume of >75%. The aW-SIRT algorithm has proven to be a valuable technique, which is applicable in reconstruction problems with flexible and complex geometry. Although the results in this work are obtained using XRIIs, the method readily applies to flat-panel detectors as well.

Acknowledgments

This research was funded by a grant from the special research fund of the University of Antwerp (BOF-GOA 2016 33927). Ellen Goossenaerts of the Veterinary Sciences Department of the University of Antwerp is acknowledged for providing the rabbit specimen. Wim Huyge is acknowledged for fabricating the PVC tube phantom. Jonathan Sanctorum, Tim Elberfeld, and Jens Renders from Imec-Visionlab are acknowledged for their support in using the ASTRA toolbox.

Conflict of interest

The authors have no conflict to disclose.

References

Aarle W van, Palenstijn W J, Cant J, Janssens E, Bleichrodt F, Dabravolski A, Beenhouwer J D, Batenburg K J and Sijbers J 2016 Fast and flexible X-ray tomography using the ASTRA toolbox *Opt. Express, OE* **24** 25129–47

van den Bergh E and Friedlander M P 2013 Spot – A Linear-Operator Toolbox Online: https://www.cs.ubc.ca/labs/scl/spot/

Bian J, Wang J, Han X, Sidky E Y, Shao L and Pan X 2012 Optimization-based image reconstruction from sparse-view data in offset-detector CBCT *Phys. Med. Biol.* **58** 205

Bleichrodt F, van Leeuwen T, Palenstijn W J, van Aarle W, Sijbers J and Batenburg K J 2016 Easy implementation of advanced tomography algorithms using the ASTRA toolbox with Spot operators *Numerical Algorithms* **71** 673–97

Cho P S, Ruddt A D and Johnson R H 1996 Cone-beam CT from width-truncated projections *Comput Med Imaging Graph* **20** 49–57

Dewaele P, Vuylsteke P, Van de Velde S and Schoeters E P 1999 Full-leg/full-spine image stitching: a new and accurate CR-based imaging technique Medical Imaging '99 ed K M Hanson (San Diego, CA) pp 131–8 Online: http://proceedings.spiedigitallibrary.org/proceeding.aspx?articleid=980546

Feldkamp L A, Davis L C and Kress J W 1984 Practical cone-beam algorithm *Journal of the Optical Society of America A* **1** 612

Gregor J and Benson T 2008 Computational Analysis and Improvement of SIRT *IEEE Transactions on Medical Imaging* **27** 918–24

Hansis E, Bredno J, Sowards-Emmerd D and Shao L 2010 Iterative reconstruction for circular cone-beam CT with an offset flat-panel detector *IEEE Nuclear Science Symposuim Medical Imaging Conference* IEEE Nuclear Science Symposuim Medical Imaging Conference pp 2228–31

Kak A C and Slaney M 1988 *Principles of computerized tomographic imaging* (New York: IEEE Press)

Krebs J, Shankar A, Bednarek D R and Rudin S 2018 Gantry rotational motion-induced blur in cone-beam computed tomography *Proc SPIE Int Soc Opt Eng* **10573** Online: https://www.ncbi.nlm.nih.gov/pmc/articles/PMC6004603/

Mettivier G, Russo P, Lanconelli N and Meo S L 2012 Cone-beam breast computed tomography with a displaced flat panel detector array *Medical Physics* **39** 2805–19

Nguyen V, De Beenhouwer J, Sanctorum J G, Van Wassenbergh S, Bazrafkan S, Dirckx J J J and Sijbers J 2020 A low-cost geometry calibration procedure for a modular cone-beam X-ray CT system *Nondestructive Testing and Evaluation* 1–14

Nguyen V, Sanctorum J G, Van Wassenbergh S, Dirckx J J J, Sijbers J and De Beenhouwer J 2021 Geometry Calibration of a Modular Stereo Cone-Beam X-ray CT System *Journal of Imaging* **7** 54

Parker D L 1982 Optimal short scan convolution reconstruction for fan beam CT *Medical Physics* **9** 254–7

Sanctorum J G, Adriaens D, Dirckx J J J, Sijbers J, Van Ginneken C, Aerts P and Van Wassenbergh S 2019 Methods for characterization and optimisation of measuring performance of stereoscopic x-ray systems with image intensifiers *Meas. Sci. Technol.* **30** 105701

Sanctorum J G, Van Wassenbergh S, Aerts P and Dirckx J J J 2020a Technical Note: Correction of geometric x-ray image intensifier distortion based on digital image correlation *Medical Physics* **47** 597–603

Sanctorum J G, Van Wassenbergh S, Nguyen V T H, De Beenhouwer J, Sijbers J and Dirckx J J J 2020b Projection-angle-dependent distortion correction in high-speed image-intensifier-based x-ray computed tomography *Measurement Science and Technology* Online: https://iopscience.iop.org/article/10.1088/1361-6501/abb33e

Schäfer D, Grass M and Haar P van de 2011 FBP and BPF reconstruction methods for circular X-ray tomography with off-center detector *Medical Physics* **38** S85–94

Sharma K S, Gong H, Ghasemalizadeh O, Yu H, Wang G and Cao G 2014 Interior micro-CT with an offset detector *Med Phys* **41** Online: https://www.ncbi.nlm.nih.gov/pmc/articles/PMC4039736/

Shepp L A and Logan B F 1974 The Fourier reconstruction of a head section *IEEE Transactions on Nuclear Science* **21** 21–43

Vedantham S, Tseng H-W, Konate S, Shi L and Karellas A 2020 Dedicated cone-beam breast CT using laterally-shifted detector geometry: Quantitative analysis of feasibility for clinical translation *Journal of X-Ray Science and Technology* **28** 405–26

Wang G 2002 X-ray micro-CT with a displaced detector array *Medical Physics* **29** 1634–6

Wang J and Blackburn T J 2000 The AAPM/RSNA Physics Tutorial for Residents *RadioGraphics* **20** 1471–7

Wang J, Zhang X, Sun Z and Yuan F 2018 An efficient intensity-based ready-to-use X-ray image stitcher *The International Journal of Medical Robotics and Computer Assisted Surgery* **14** e1925

Yu L, Pelizzari C, Pan X, Riem H, Munro P and Kaissl W 2004 Application of asymmetric cone-beam CT in radiotherapy *IEEE Symposium Conference Record Nuclear Science 2004.* IEEE Symposium Conference Record Nuclear Science 2004. vol 5 pp 3249-3252 Vol. 5